Temperature-dependent elasticity of $Pb[(Mg_{0.33}Nb_{0.67})_{1-x}Ti_x]O_3$

Sumudu Tennakoon,[1,*] Joseph Gladden,[2,3,†] Mainak Mookherjee,[1,‡] Tiglet Besara,[4] and Theo Siegrist[4,5]

[1]*Earth Materials Laboratory, Department of Earth, Ocean and Atmospheric Sciences, Florida State University, Tallahassee, Florida 32306, USA*

[2]*Department of Physics and Astronomy, University of Mississippi, University, Mississippi 38677, USA*

[3]*National Center for Physical Acoustics, University of Mississippi, University, Mississippi 38677, USA*

[4]*National High Magnetic Field Laboratory, Tallahassee, Florida 32310, USA*

[5]*FAMU-FSU College of Engineering, Tallahassee, Florida 32310, USA*

(Received 2 May 2017; published 13 October 2017)

Relaxor ferroelectric materials, such as $Pb[(Mg_{0.33}Nb_{0.67})_{1-x}Ti_x]O_3$ (PMN-PT) with generic stoichiometry, undergo a ferroelectric-to-paraelectric phase transition as a function of temperature. The exact transition characterized by Curie temperature (T_c) varies as a function of chemistry (x), i.e., the concentration of Ti. In this study, we investigated the structural phase transition by exploring the temperature dependence of the single-crystal elastic properties of $Pb[(Mg_{0.33}Nb_{0.67})_{0.7}Ti_{0.3}]O_3$, i.e., $x \approx 0.3$. We used resonant ultrasound spectroscopy to determine the elasticity at elevated temperatures, from which $T_c = 398 \pm 5$ K for PMN-PT ($x \approx 0.3$) was determined. We report the full elastic constant tensor ($C_{ij} = \{C_{11}, C_{12}, C_{44}\}$), acoustic attenuation (Q^{-1}), longitudinal (V_P) and shear (V_S) sound velocities, and elastic anisotropy of PMN-PT as a function of temperature for $400 < T < 871$ K. Temperature trends of the elastic constants C_{11}, C_{44} and bulk modulus indicate that at $T > T_c$ the material first stiffens and reaches maxima in the vicinity of the Burns temperature ($T_b \sim 673$ K), followed by a more typical gradual softening of the elastic constants. Similar temperature-dependent anomalies are also observed with anisotropy and Q^{-1}, with minima in the vicinity of T_b. We used the temperature dependence of C_{ij}, Q^{-1}, V_P, V_S, and anisotropy to infer the evolution of polar nanoregions as the material evolved from $T > T_c$.

DOI: 10.1103/PhysRevB.96.134108

I. INTRODUCTION

Lead magnesium niobate-lead titanate (PMN-PT) is a relaxor ferroelectric material that belongs to a subfamily of lead-based complex perovskites. Perovskites have ABO_3 stoichiometry, where the A sites have 12-fold coordination and the B-sites have 6-fold octahedral coordination. In PMN-PT perovskites, the Pb atoms are in the A site, and the B site is either occupied by Ti atoms as in $PbTiO_3$ or by a pair of low- and high-valency atoms with a general stoichiometry of $Pb[(B_l^{\alpha+})_\delta(B_h^{\beta+})_{1-\delta}]O_3$ [1]. The subscript "l" in "B_l" refers to the low-valency sites and is typically occupied by Mg, Zn, Ni, Zr, In, Fe, Sc, and Y cations. The subscript "h" in "B_h" refers to the high-valency sites and is typically occupied by Nb, Ta, and W cations [1]. The charge balance in the crystal structure is maintained by the relation $\delta\alpha + (1-\delta)\beta = 4$. B_l and B_h sites in the $Pb(Mg_{0.33}Nb_{0.67})O_3$ crystal structure are occupied by Mg and Nb, respectively, i.e., with a δ of 1/3. PMN-PT is a solid solution with a general stoichiometry of $Pb[(Mg_{0.33}Nb_{0.67})_{1-x}Ti_x]O_3$, where, $x = 0$ and 1 refers to the end members $Pb(Mg_{0.33}Nb_{0.67})O_3$ (PMN) and $PbTiO_3$ (PT), respectively. Single crystal of PMN-PT can be synthesized at high temperatures (≈1300 K) [2].

Below the Curie temperature (T_c), uniformly aligned electric dipoles in relaxor ferroelectric materials are arranged to form several domains, which in turn generates spontaneous polarization. Polarizations of these domains can be altered by application of an external electric field. At temperatures, greater than T_c, the ferroelectric phase transforms to the paraelectric phase, accompanied by a reduction in the size of the polarized domains to randomly oriented polar nanoregions (PNRs). PNRs, however, do affect the bulk properties of the material such as elasticity [3,4]. At higher temperatures, i.e., $T > T_b$ (T_b = Burns temperature), the PNRs are eventually fully depleted and the material becomes paraelectric. The Burns temperature for $Pb[(Mg_{0.33}Nb_{0.67})_{1-x}Ti_x]O_3$ with $x = 0$ and 0.30 is 623 and 673 K, respectively [5–7]. For $Pb[(Mg_{0.33}Nb_{0.67})_{1-x}Ti_x]O_3$ compositions with $x > 0.3$, T_b is slightly affected by varying x [8] and $T_b > T_c$ by ≈270 K. Relaxor ferroelectrics are often good piezoelectric materials below the T_c, with the temperature-dependent dielectric response defined by a broad peak with a maximum at T_m, and it is also dependent on frequency. This is in contrast to the well-defined and sharp peak observed for regular ferroelectrics [9].

In the temperature-composition (T-x) diagram for PMN-PT, the relaxor PMN phase ($x = 0$) is rhombohedral with $R3m$ space-group symmetry below the T_c [3,10–14], while the ferroelectric PT phase ($x = 1.0$) is tetragonal with $P4mm$ space-group symmetry [3,10–13]. The composition range with $0.30 < x < 0.35$ is often described as the morphotropic phase boundary (MPB) of PMN-PT [3,10,11] and is characterized by the abrupt changes in the crystal structure and piezoelectric properties [3,15–18]. PMN-PT phases with monoclinic and orthorhombic space-group symmetries have been reported in the vicinity of the MPB [19–22]. At T_c, the PMN-PT crystal undergoes a structural phase transition to cubic space-group symmetry $Pm\bar{3}m$ [3]. This ferroelectric-to-paraelectric phase-transition temperature varies linearly with composition (x). The ferroelectric-paraelectric transition temperatures for the end members PMN and PT are 283 and 765 K, respectively [3,10,11], whereas the transition temperature in the vicinity

*stennakoon@fsu.edu
†jgladden@olemiss.edu
‡mmookherjee@fsu.edu

of the MPB region is around 400 K [3,10–12,23]. The PMN-PT phases at and near the MPB region ($0.30 < x < 0.35$) have been studied extensively due to their unusually large electromechanical properties, i.e., piezoelectric coefficients $d_{33} = 1500$–$2500\,\mathrm{pC/N}$ and an electromechanical coupling factor of $k_{33} > 0.9$ [15,24]. PMN-PT crystals find applications in transducers in highly sensitive broadband acoustic devices, actuators, and energy-harvesting devices [2,3,15].

It is well known that structural phase transitions often manifest themselves in changes in elasticity [25–29]. Although PMN-PT is an extensively studied material, the temperature dependence of the single-crystal elasticity of PMN-PT remains largely unexplored. Only the room-temperature elasticity for PMN-PT has been reported [30–33] (Table I). Here, we explore the temperature-dependent elasticity, the elastic anisotropy, and the acoustic attenuation of PMN-PT crystal across a wide range of temperatures (400–871 K), and we relate our temperature-dependent elasticity results to the structural changes associated with the ferroelectric transition in PMN-PT.

II. MATERIALS AND METHODS

We obtained the PMN-PT crystals from the H.C. Materials Corp. Unpolarized single crystals of PMN-PT were grown using the Bridgeman method [2,33]. We cut precise rectangular parallelepiped samples of dimensions of $0.3540(5) \times 0.2580(5) \times 0.1990(5)$ cm using a South Bay Technologies 660 slow speed diamond wheel saw. We polished the sample faces using a lapping machine to a smooth optical quality surface. We used single-crystal x-ray diffraction at National Magnetic High Field Laboratory, Florida State University to verify that the [001], [010], and [001] crystal axes were oriented parallel to the axial directions of the rectangular parallelepiped. We used powder x-ray diffraction to determine the space-group symmetry (*R3m*) and lattice parameters of the sample, which are $a = b = c = 4.019\,64(2)$ and $\alpha = \beta = \gamma = 89.894(4)$ (Fig. SF1a in the Supplemental Material [34]). The mass of the sample is 0.1460(1) g and the corresponding density is $8.04(5)\,\mathrm{g\,cm^{-3}}$. The measured density agrees with a previous study on PMN-PT of similar composition [31]. We also determined the stoichiometry of the sample using energy-dispersive x-ray spectroscopy in a scanning electron microscope (SEM-EDS) at the Condensed Matter and Materials Physics Facility, Department of Physics, Florida State University. The PMN-PT sample used in our study has a stoichiometry of $Pb[(Mg_{0.33}Nb_{0.66})_{0.7}Ti_{0.3}]O_3$.

We used resonant ultrasound spectroscopy (RUS) at the National Center for Physical Acoustics (NCPA), University of Mississippi to determine the elastic constants in the temperature range of 293–871 K, by utilizing the mechanical resonance spectra (MRS) of the solid sample. The MRS consist of a set of natural frequencies, which are influenced by the elastic constant tensor (C_{ij}), density (ρ), and geometry of the sample. The elastic constants are in turn influenced by the crystal structure. Resonance occurs when the excitation frequency (f) equals a natural frequency (f_0) of the sample. The vibrations are amplified approximately by the quality factor of the resonances ($Q = f_0/\Delta f$), where Δf is the full width at half-maximum for the resonance frequency. The maximum number of modes observed in the MRS is ~ 21, of which we used 16 modes across all temperatures for the determination of elastic constants. We predicted the normal mode frequencies f_i^{calc} ($i = 1,2,\ldots$) of the PMN-PT following the Rayleigh-Ritz method [26,28,35–39]. We use the least-squares method to minimize ΔF, defined as $\sqrt{\frac{1}{N}\sum_{i=1}^{N}\left(\frac{f_i^{\mathrm{obs}} - f_i^{\mathrm{calc}}}{f_i^{\mathrm{calc}}}\right)^2} \times 100\%$, where the f_i^{obs} and f_i^{calc} are observed and calculated resonance frequencies. We calculate the resonance frequencies based on an initial guess of elastic constants (C_{ij}). Our MRS spectra have $\Delta F < 0.45\%$ (400–500 K) and it is ≈ 0.3 at $T > 500$ K. We determine the uncertainty for the elastic moduli (δC_{ij}) from the effective curvature ($\frac{df}{dC_{ij}}$) of the minima in elastic moduli. Our error estimates for the elastic constants are $\delta C_{11} < 2\%$, $\delta C_{12} < 3\%$, and $\delta C_{44} < 0.3\%$.

In the RUS experimental setup, we placed our sample between two lithium niobate ($LiNbO_3$) piezoelectric transducers (Fig. SF1b in the Supplemental Material [34]). A Stanford Research Systems (SRS) DS345 function generator was used to excite one of the transducers in contact with the sample with a sweeping sinusoidal signal. The other transducer was connected to an SRS SR844 lock-in amplifier that monitors the vibration response of the sample. A thermocouple is placed in proximity to the sample. The sample and the surrounding ceramic framework are placed in a fused quartz tube and then inserted in the high-temperature furnace (Carbolite MTF 12/28/250). In our high-temperature experiments, we maintained temperatures within ± 1 K using a proportional integral derivative controller. An inert gas flushing system is employed to maintain the oxygen content at low levels (<20 ppm) to minimize the oxidation reaction of the sample, transducer, and electrical contacts [26,40].

At temperatures below 400 K, i.e., $T < T_c$, the MRS show significant peak broadening and a low signal-to-noise ratio (SNR), making it difficult to extract meaningful information on elastic constants at $T < T_c$. Hence, we conducted pulse-echo (PE) measurements on our PMN-PT sample to determine the elastic constant at room temperature [41,42]. We used an Olympus 5072PR pulsar-receiver to generate ultrasonic pulses (Fig. SF1c in the Supplemental Material [34]). To measure the longitudinal wave speed (V_P), we used an ultrasonic gel to couple a 10 MHz longitudinal transducer (Olympus V112) to the sample. To measure the shear wave speed (V_S), we used commercially available shear viscous gel to couple a 5 MHz shear transducer (Olympus V156) to the sample. We used a Tektronix TDS3000B digital oscilloscope to measure the pulse-echo signal in the time domain. We measured the wave speed along the [001] direction of the cubic PMN-PT crystal. We determined V_P and V_S using the relation between the travel time (Δt) and the sample thickness ($d = 2$ mm) as $V = \frac{2d}{\Delta t}$. We derived elastic constants (C_{33}) and (C_{44}) from the measured speeds along [001] directions using the formulas $V_{P[001]} = \sqrt{\frac{C_{33}}{\rho}}$ and $V_{S[001]} = \sqrt{\frac{C_{44}}{\rho}}$, where ρ is the density.

III. RESULTS AND DISCUSSION

At room temperature, the symmetry of PMN-PT ($x \approx 0.3$) is pseudocubic [43], i.e., with three distinct elastic constants C_{11}, C_{12}, and C_{44}. We measured the longitudinal (V_P) and

TABLE I. Room-temperature elastic constants (C_{ij}) across the PMN-PT solid solutions and from this study PMN-PT ($x \approx 0.3$). The elastic constants are reported in GPa. PE refers to pulse echo and RUS refers to resonant ultrasound spectroscopy.

	C_{11}	C_{12}	C_{13}	C_{33}	C_{44}	C_{66}	K_H	G_H	Source
PT ($x = 1.00$)	237	90	70	60	69	104	85	55	[61]
PMN ($x = 0.00$)	156	76			69		103	55	[18]
PMN-PT ($x = 0.29$)	124	111	104	108	63	35	93	30	[33]
PMN-PT ($x = 0.30$)	117	103	101	108	71	66	105	29	[32]
PMN-PT ($x = 0.33$)	115	103	102	103	69	66	104	25	[31]
PMN-PT ($x = 0.42$)	175	85	83	105	28	80	102	37	[31]
PMN-PT ($x \approx 0.30$)									
293 K				124.0	62.5				This work (PE)
PMN-PT ($x \approx 0.30$)									This work (RUS)
412 K	134.2	89.4			66.3		104.4	43.0	
443 K	157.8	87.7			74.5		111.1	55.0	
473 K	167.5	83.2			78.0		111.3	60.9	
493 K	174.4	83.9			77.8		114.1	62.6	
513 K	177.3	83.4			78.4		114.7	63.8	
572 K	183.3	84.7			78.8		117.6	65.3	
594 K	184.6	85.3			78.8		118.4	65.5	
671 K	185.7	86.1			78.5		119.3	65.4	
771 K	184.3	85.9			78.0		118.7	64.8	
872 K	181.5	85.6			77.0		117.6	63.7	

transverse (V_S) velocity along the [001] direction and deduced C_{44} and C_{33} (where $C_{33} \approx C_{11}$) (Table I). It is expected that at room temperature, i.e., $T < T_c$, the single crystal PMN-PT is twinned due to the lowering of the symmetry to the rhombohedral space group ($R3m$) from the cubic space group ($Pm\bar{3}m$). Thus, we examined the single-crystal diffraction pattern of the PMN-PT ($x \approx 0.3$) crystal at room temperatures. We were, however, unable to observe distinct evidence of twinning based

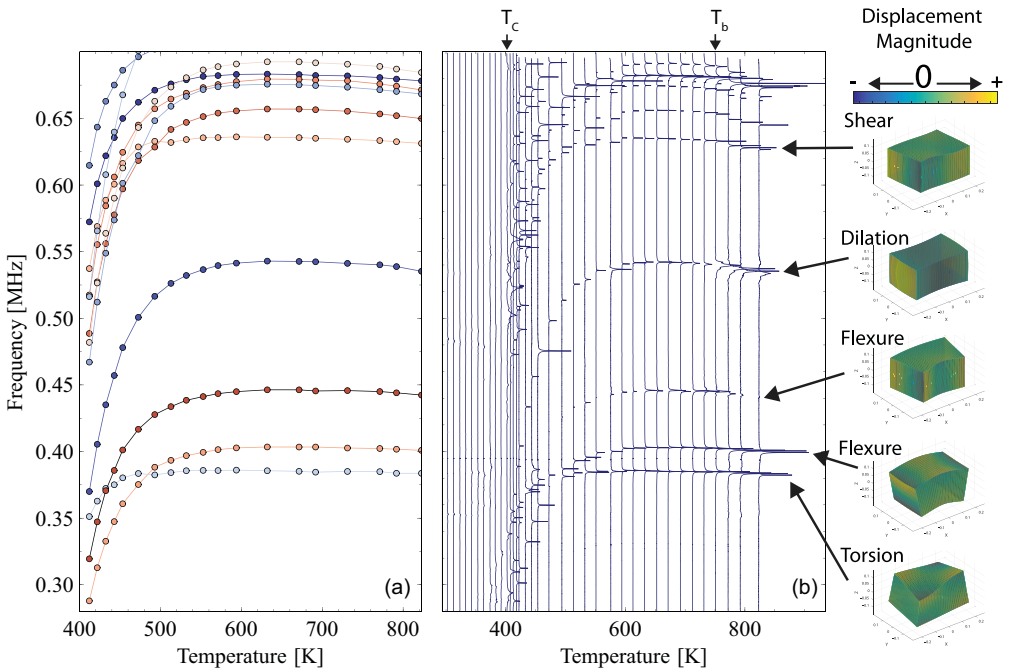

FIG. 1. (a) Temperature dependence of the first ten mechanical resonance frequencies. (b) Temperature evolution of MRS from 290 to 823 K. For the PMN-PT sample ($x \approx 0.3$) explored in this study, a distinct transition in the temperature dependence of MRS is observed at around ~400 K, i.e., (T_c). Mode displacement plots [62] of the first five resonance modes of the PMN-PT sample are also shown and indicated by arrows with the corresponding modes in (b).

on the room-temperature single-crystal x-ray diffraction. The elasticity results of twinned crystals may require additional data analysis [44]. We determined the elastic constants of PMN-PT ($x \approx 0.3$) at room temperature assuming an untwinned crystal, and our values are in good agreement with previous studies on PMN-PT from the MPB region (Table I). At higher temperatures, i.e., $T > T_c$, the symmetry is cubic and the crystal becomes untwinned. We collected MRS of the PMN-PT ($x \approx 0.3$) crystal from room temperature (293 K) up to 871 K (Fig. 1). In the temperature range of 373–423 K, we observe an abrupt change in the MRS at ~398 $\pm$ 5 K. This is defined as the Curie transition temperature (T_c), where the ferroelectric-to-paraelectric phase transition occurs in PMN-PT. This transition temperature compares favorably to the ferroelectric phase-transition temperature (T_c) of PMN-PT with compositions $x \approx 0.3$ [10,11,23,45,46]. At $T > T_c$, we note a monotonic increase in the resonance mode frequencies (f_i) with the temperature indicating stiffening of the material. The temperature dependence of the f_i shows a significant variation in their temperature maxima in the range 600–673 K. We do not observe any hysteresis in f_i upon multiple heating and cooling cycles, i.e., the PMN-PT sample undergoes a reversible change in the explored temperature range.

In the temperature range of 400–673 K, we observe a nonlinear increase in the longitudinal (C_{11}) and shear elastic constants C_{44} by 40% and 33%, respectively. In contrast, the off-diagonal elastic constant C_{12} decreases upon heating, reaching a minimum at 493 $\pm$ 20 K, and then it increases upon further heating (Fig. 2).

We define the average acoustic energy loss for all the modes, $Q_{\text{av}}^{-1} = \sum_i^N Q_i^{-1}/N$, where Q_i^{-1} refers to the acoustic energy loss of an individual mode, and N is the total number of modes considered in this study, i.e., 16. We identify three distinct regions marked "1," "2," and "3" in the temperature dependence of Q_{av}^{-1} (Fig. 2). The three distinct temperature regions relate to the dissipation of energy due to the presence of randomly oriented polar nanoregions. In the region "1," i.e., $412 < T < 450$ K, the Q_{av}^{-1} reduces by ~75%; in the region "2," i.e., $450 < T < T_b$, the Q_{av}^{-1} remains constant within 25 $\pm$ 5% of the Q_{av}^{-1} at $T = 412$ K; and finally, in the region "3," at $T > T_b \sim 673$ K, Q_{av}^{-1} increases linearly.

By examining the plots of the mode displacement field and the parity group (k value) of the mode, we categorized the measured sample resonance mode into modes related to torsion, flexure, shear, and dilation [35,36,47]. We labeled the resonant modes of PMN-PT as FZ-1: the lowest-order flexure mode in the Z direction; SY-1: the lowest-order shear mode in the Y direction; DO-1: the lowest-order dilation mode; and TO-1: the lowest-order torsion mode (Fig. 1). We used the derivative $\frac{df}{dC_{ij}}(ij = \{11, 12, 44\})$ of each mode to relate the dominant elastic constants, as the lower-order resonance modes are often related to a single elastic constant. For instance, the FX-1, FY-1, FZ-1, and DO-1 modes are likely to be related to C_{11}. The TO-1, TO-2, SX-1, and SZ-1 modes are likely to be related to C_{44}, Similarly, the higher-order modes are often related to a combination of elastic constants. The TO-1, TO-2, SX-1, and SZ-1 modes related to C_{44} showed similar temperature dependences with maxima at 570 $\pm$ 20 K, whereas the FX-1, FY-1, FZ-1, and DO-1 modes related to

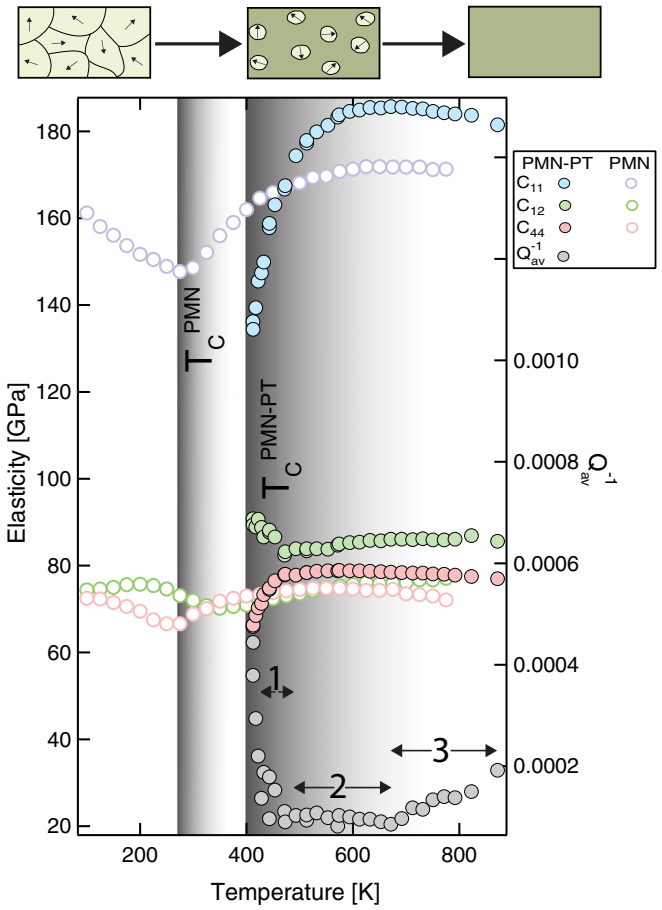

FIG. 2. Temperature dependence of C_{11}, C_{12}, C_{44}, and acoustic energy loss (Q_{av}^{-1}) of the same sample measured in two different temperature cycles. Also shown are the elastic constants for PMN ($x = 0.0$) [14,58]. The two gray and white shaded regions shown in the figure indicates the ferroelectric-to-paraelectric transition with T_c for PMN and for PMN-PT. The T_c for PMN is ~270 K, whereas the T_c for PMN is ~398 K.

C_{11} showed similar temperature dependences with maxima at 650 $\pm$ 20 K (Fig. 2). The linear behavior of the elastic constants at temperatures above T_b can be attributed to the lattice anharmonicity in the paraelectric phase of the material.

We calculated the isotropic bulk modulus (K_H) and the shear modulus (G_H) using the measured elastic constants, C_{ij}'s, following the Voigt-Reuss-Hill (VRH) approximations (Table I) [48,49].

The Hill-averaged bulk modulus (K_H) and shear modulus (G_H) for cubic crystals are defined as $K_H = \frac{1}{2}(K_V + K_R)$ and $G_H = \frac{1}{2}(G_V + G_R)$, where the subscript V refers to Voigt-averaged, $K_V = \frac{(C_{11}+2C_{12})}{3}$, and the subscript R refers to Reuss-averaged, $K_R = \frac{1}{(3S_{11}+6S_{12})}$, $G_V = \frac{(C_{11}-C_{12})+3C_{44}}{5}$, and $G_R = \frac{5}{4(S_{11}-S_{12})+3S_{44}}$. The components of the compliance tensor (S_{ij}) are obtained from $[S_{ij}] = [C_{ij}]^{-1}$. We used isotropic K_H and G_H values in the following equation to calculate Poisson's ratio: $\nu = \frac{(3K_H - 2G_H)}{2(3K_H + G_H)}$. The isotropic Poisson ratio (ν) decreased in the temperature range of 400–530 K with a minimum observed at 530 K. Above 530 K, ν gradually increases linearly (Fig. SF2 of the Supplemental Material [34]).

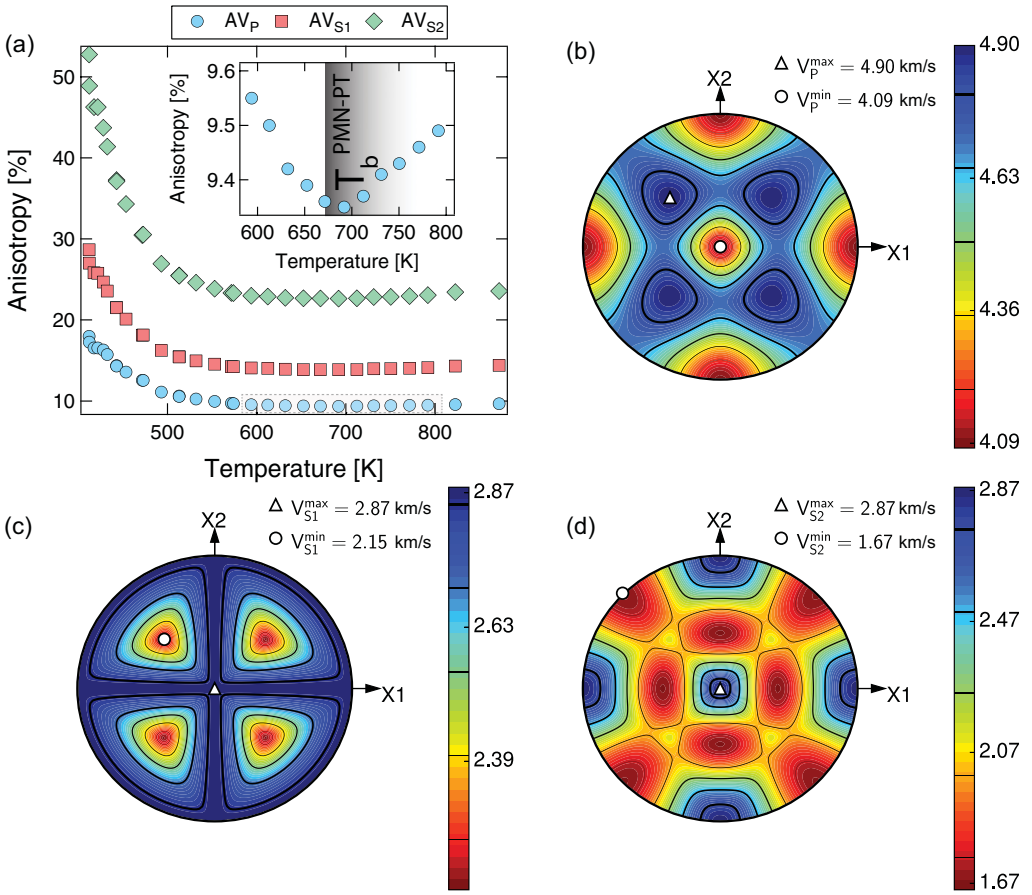

FIG. 3. (a) The plot shows the temperature dependence of the sound velocity anisotropy: AV_P, AV_{S1}, and AV_{S2}. We define the anisotropy $AV_P = \frac{200 \times (V_{P\max} - V_{P\min})}{(V_{P\max} + V_{P\min})}$ and $AV_S = \frac{200 \times (V_{S\max} - V_{S\min})}{(V_{S\max} + V_{S\min})}$. The inset shows the inflection in AV_P at the Burns temperature, T_b; (b)–(d) are the stereographic plots of the directional dependence of sound velocities: V_p, V_{s1}, and V_{s2} at 412 K.

We used polycrystalline aggregate elastic moduli to determine the longitudinal, $V_P = \sqrt{\frac{K_H + \frac{4}{3}G_H}{\rho}}$, and shear, $V_S = \sqrt{\frac{G_H}{\rho}}$, sound-wave velocities as functions of temperature (Fig. SF2 of the Supplemental Material [34]). To analyze the sound-wave velocities as functions of the propagating direction in the crystal, we applied the full elastic tensor of PMN-PT ($x \approx 0.3$) obtained from the RUS measurements in solving the Christoffel equation [50,51]:

$$\sum_{ij}[M_{ij} - V^2\delta_{ij}]p_j = 0,$$

where V is the sound velocity,

$$M_{ij} = \sum_{nm} k_n C_{ijkl} k_m,$$

$$\delta_{ij} = \begin{cases} 1, & i = j \\ 0 & \text{otherwise} \end{cases}$$

$$\vec{k} = (k_1, k_2, k_3)$$

are unit vectors along propagation directions, and $\vec{p} = (p_1, p_2, p_3)$ are polarization vectors. A stereographic projection of the longitudinal sound velocity (V_P), the two transverse shear velocities, V_{S1} and V_{S2}, demonstrate the cubic space-group symmetry of the PMN-PT crystal (Fig. 3). We also observed that the sound velocity anisotropies (AV_P, AV_{S1}, and AV_{S2}) of PMN-PT reduce asymptotically at higher temperature and exhibit minima at the Burns temperature, i.e., $T_b \approx$ 673 K(Fig. 3).

For the PMN-PT ($x \approx 0.3$) phase, at temperatures below $T_c < 400$ K, the microstructure consists of ferroelectric domains with spontaneous polarization. The size of these domains is often of micrometer scale [52] and they cause dissipation of acoustic energy, which results in weakening of the resonance peaks in the MRS. The difficulty in acquiring elasticity measurement by the RUS method at temperatures below T_c is also known for several other relaxor ferroelectrics, including $Pb(In_{0.5}Nb_{0.5})O_3$-$Pb(Mg_{0.33}Nb_{0.67})O_3$-$PbTiO_3$ (PIN-PMN-PT) [27], $Ca_{0.28}Ba_{0.72}Nb_2O_6$ (CBN) [53,54], $LaAlO_3$ [55], and $KTa_{1-x}Nb_xO_3$ (KTN) [25]. In PMN-PT relaxor ferroelectrics, for compositions toward the PMN end, i.e., between $x \approx 0.0$ and $x \approx 0.3$ as the temperature surpasses T_c, these ferroelectric domains are severely reduced and the crystal structure gradually transitions from the rhombohedral space-group symmetry to a pseudocubic symmetry structure, which eventually transitions to a cubic space-group symmetry [10,56,57]. An ordinary ferroelectric material becomes paraelectric at $T > T_c$, but in the case of relaxors, polar nanoregions (PNRs) with randomly oriented local polarization

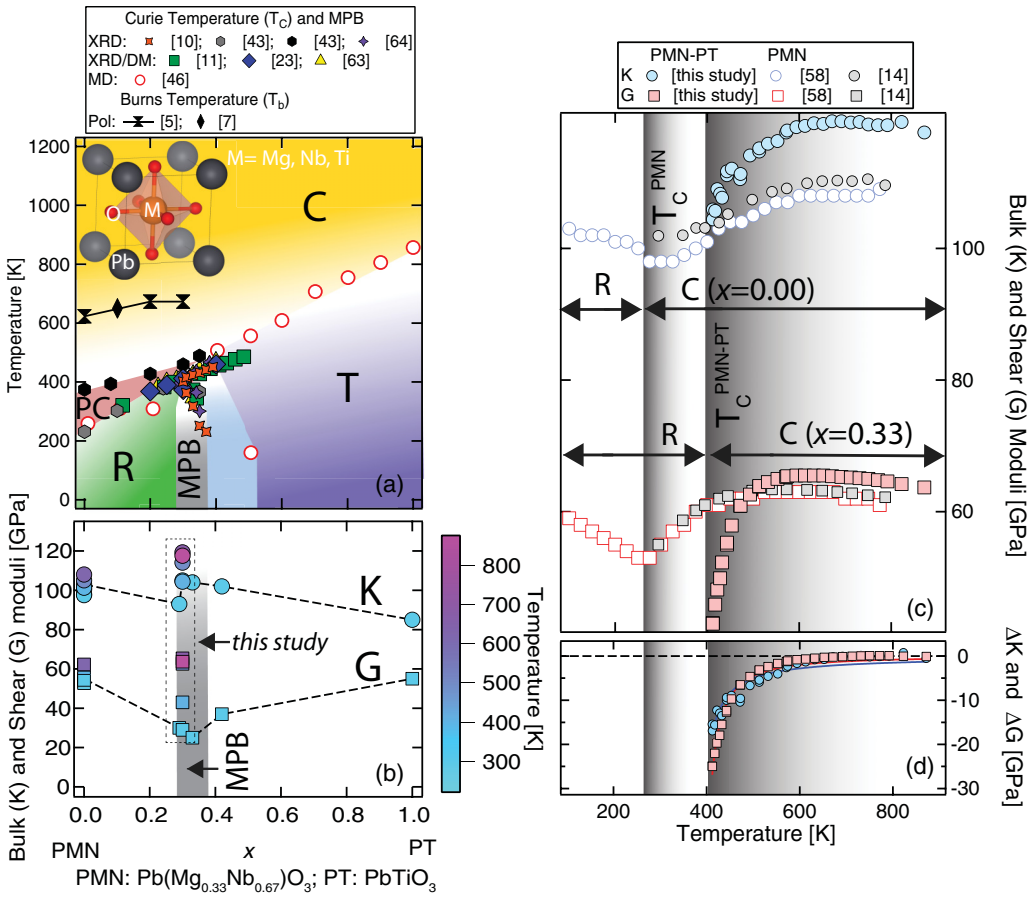

FIG. 4. (a) Temperature-composition ($T-x$) phase diagram for PMN-PT with a stoichiometry $Pb[(Mg_{0.33}Nb_{0.67})_{1-x}Ti_x]O_3$. The phase diagram is subdivided based on the space-group symmetry of the PMN-PT crystals. "C" refers to the cubic space-group symmetry ($Pm\bar{3}m$), "R" refers to rhombohedral space-group symmetry ($R3m$), "T" refers to tetragonal space group symmetry ($P4mm$), and "MPB" refers to the morphotropic phase boundary, which is attributed to monoclinic phases (Bm and Pm) [13]. The region "PC" refers to pseudocubic, where $a=b=c$ and $\alpha=\beta=\gamma\lesssim 90$ [43]. The phase-transition temperatures shown in the figure are from previous studies including x-ray diffraction (XRD) [10,11,43,63,64], dielectric measurements (DM) [11,23,63], and molecular-dynamics (MD) simulations [46]. The shaded region extended up to $x=0.5$ indicates the MPB determined from MD [46]. The inset shows the crystal structure of a PMN-PT phase with cubic space-group symmetry ($Pm\bar{3}m$). Dashed lines indicate the compositional variation of Burns temperature (T_b) [5,7]. (b) Bulk (K) and shear (G) moduli as a function of x. Room temperature K and G are connected with dashed lines. Color scale indicates the temperatures. (c) Bulk (K) and shear (G) moduli of PMN ($x=0$) [58] and PMN-PT ($x=0.3$) as a function of temperature. T_c for PMN and PMN-PT ($x=0.3$) is also marked in the plot. (d) ΔK and shear ΔG as a function of temperature. The blue and red lines represent fits $[A(T-T_f)^{\kappa}]$ to the ΔK and ΔG with $T_f=380$ K [22]. The fitted parameter A for ΔK and ΔG are -499 and -2974 GPa, respectively. The fitted parameter K for ΔK and ΔG are -0.96 and -1.36, respectively. The two gray and white shaded regions shown in the figure indicate the ferroelectric-to-paraelectric transition with the T_c for PMN and for PMN-PT.

exist at $T_c < T < T_b$ [5] (Fig. 2). These PNRs are reduced with increasing temperature, and at temperatures $T > T_b$ the PNRs eventually vanish and the crystal loses any local polarization. The T_b for PMN-PT is determined [5] based on the temperature dependence of the strain, the thermal expansion coefficient, and the magnitude of the polarization. The transition from PNR to complete loss of polarization is well documented in the transition between regions "2" and "3" in the plot of Q_{av}^{-1} versus temperature (Fig. 2). The temperature dependence of elasticity in the PMN-PT from this study compares well with RUS results of other relaxor ferroelectrics including PIN-PMN-PT [27], CBN [54,53], and KTN [25].

We compared the room-temperature elasticity, i.e., bulk and shear moduli across the PMN-PT solid solution [Figs. 4(a) and 4(b)]. We note that the bulk modulus decreases from the PMN end member and reaches a minimum at the morphotropic phase boundary, i.e., PMN-PT with $x=0.3$. At $x>0.3$, the bulk modulus is larger and then it reduces monotonically toward the PT ($x=0.3$) [Fig. 4(b)]. The variation of the shear modulus across the PMN-PT solid solution shows a clear minimum at the morphotropic boundary, i.e., PMN-PT with $x=0.3$. Both of the end member compositions, i.e., PMN ($x=0.0$) and PT ($x=1.0$), have shear moduli greater than at MPB [Fig. 4(b)].

The temperature dependence of these isotropic moduli is shown in Fig. 4(c). In the PMN-PT ($x=0.3$) crystal, we observe that the bulk, K_H, and shear, G_H, moduli stiffen at high temperature up to $\approx T_b$, followed by a gradual softening. However, the maxima in the temperature dependence of the bulk, K_H, and shear, G_H, moduli occur at different temperatures of 673 ± 20 and 623 ± 20 K, respectively. We

compared the high-temperature elasticity of PMN-PT with previous studies on PMN using ultrasonic speed of sound measurements [58], Brillouin scattering [59,60], and RUS [14]. We note that the ferroelectric-to-paraelectric transition temperature (T_c) varies as a function of composition of PMN-PT. For instance, for PMN ($x = 0.0$) and PMN-PT ($x = 0.3$), T_c is 270 K and 398 $\pm$ 5 K, respectively. We note that T_c increases from PMN to PT [Figs. 4(a) and 4(c)]. At the PMN end member, the octahedral sites are occupied by both Mg and Nb cations. At $T < T_c$, the Mg and Nb cations move along the [111] direction, i.e., one threefold axis of the cube, and they lower the cubic symmetry to rhombohedral symmetry. As the Ti concentration increases in the octahedral site, the PMN-PT crystal structure stabilizes in the tetragonal space-group symmetry at $T < T_c$ due to the displacement of Ti along the [001] direction. At $T < T_c$, the morphotropic phase boundary is a special region in between the rhombohedral space-group symmetry at the PMN-rich end member and the tetragonal symmetry toward the PT-rich end member. At MPB, the octahedral site in PMN-PT is almost half-occupied by Nb (0.47), and the remaining half of the octahedral site is occupied by a combination of Ti (0.30) and Mg (0.23). Based on the temperature dependence of the bulk and shear moduli, the difference between elastic constants at T_b and T_c can be estimated. We find that the change in bulk (K) and shear (G) moduli is $\approx$18 and $\approx$24 GPa, respectively, for PMN-PT ($x = 0.3$). In comparison, the change in bulk (K) and shear (G) moduli is $\approx$10 and $\approx$20 GPa, respectively, for PMN ($x = 0$) [14,58–60]. The change in bulk (ΔK) and shear (ΔG) moduli is estimated by taking the difference between the bulk and shear moduli at temperatures between T_b and T_c and the linear extrapolation of the bulk and shear moduli fitted to the data at $T > T_b$. The change in bulk (ΔK) and shear (ΔG) moduli as a function of temperature is very nonlinear and can be adequately described by a power law,

$$\Delta C = A(T - T_f)^{\kappa},$$

where ΔC represents ΔK or ΔG, A and κ are material constants, and T_f is a temperature at which the nanopolar domain freezes and $T_f < T_C$ [55] [Fig. 4(d)]. So, in the composition region defined by $0.0 < x < 0.3$, we note that the addition of titanium into PMN, i.e., an increase in x, is likely to elevate the magnitude of the elasticity change (ΔC) with the ferroelectric-to-paraelectric phase transition in PMN-PT.

IV. CONCLUSIONS

We examined the temperature-dependent ferroelectric-to-paraelectric transition of PMN-PT ($x = 0.3$). Across the structural phase transition, the symmetry changes from rhombohedral to pseudocubic at T_c. Examining the temperature dependences of MRSs over the transition temperature range, we determined the ferroelectric transition temperature (T_c) of PMN-PT ($x = 0.3$) to be 398 $\pm$ 5 K. We measured the full set of elastic constants (C_{ij}) of the relaxor ferroelectric PMN-PT in the temperature range of 400–871 K. The temperature evolution of the PMN-PT elastic moduli establishes a significant stiffening in the temperature range $T_c < T < T_b$ followed by a gradual softening. In the temperature range $T_c < T < T_b$, the temperature dependences of the elastic constants C_{11}, C_{12}, and C_{44} behave in a distinct manner, likely related to the differences in sensitivity of these elastic constants to the evolution of PNRs. We report that the maxima in C_{11} and isotropic bulk modulus (K) and the minimum of the sound wave anisotropy (AV_P, AV_S) correlate with the Burns temperature ($T_b \approx 673$ K). We also detected an anomaly in the acoustic attenuation (Q^{-1}) with a broad minimum in the vicinity of T_b, followed by a linear increase at temperatures $T > T_b$. The nonlinear behavior of the elastic constants, acoustic attenuation, and elastic anisotropy of PMN-PT is attributed to the evolution of the PNRs at $T_c < T < T_b$ and their depletion at $T > T_b$.

ACKNOWLEDGMENTS

S.T. and J.G. acknowledge National Center for Physical Acoustics, University of Mississippi. S.T. acknowledges the Graduate School Dissertation Fellowship, University of Mississippi in Spring 2016. S.T. and M.M. acknowledge National Science Foundation Awards No. EAR-1639552 and No. EAR-1634422. T.B. and T.S. acknowledge support by the National Science Foundation under Contract No. DMR-1625780. A part of this work was performed at the National High Magnetic Field Laboratory (NHMFL), which is supported by National Science Foundation Cooperative Agreement No. DMR-1157490, the State of Florida, and the DOE.

[1] F. Jona and G. Shirane, *Ferroelectric Crystals* (Pergamon, New York, 1962).

[2] S. Zhang and F. Li, High performance ferroelectric relaxor-$PbTiO_3$ single crystals: Status and perspective, J. Appl. Phys. **111**, 31301 (2012).

[3] E. Araújo and E. Borges, Recent advances in processing, structural and dielectric properties of PMN-PT ferroelectric ceramics at compositions around the MPB, in *Advances in Ceramics – Electric and Magnetic Ceramics, Bioceramics, Ceramics and Environment*, edited by C. Sikalidis (InTech, Rijeka, 2011).

[4] A. A. Bokov and Z.-G. Ye, Recent progress in relaxor ferroelectrics with perovskite structure, J. Mater. Sci. **41**, 31 (2006).

[5] R. Wongmaneerung, R. Guo, A. Bhalla, R. Yimnirun, and S. Ananta, Thermal expansion properties of PMN-PT ceramics, J. Alloys Compd. **461**, 565 (2008).

[6] G. Burns and F. H. Dacol, Glassy polarization behavior in ferroelectric compounds $Pb(Mg_{1/3}Nb_{2/3})O_3$ and $Pb(Zn_{1/3}Nb_{2/3})O_3$, Solid State Commun. **48**, 853 (1983).

[7] P. M. Gehring, W. Chen, Z.-G. Ye, and G. Shirane, The non-rhombohedral low-temperature structure of PMN–10% PT, J. Phys.: Condens. Matter **16**, 7113 (2004).

[8] J.-H. Ko, D. H. Kim, S. Tsukada, S. Kojima, A. A. Bokov, and Z.-G. Ye, Crossover in the mechanism of ferroelectric phase transition of $Pb[(Mg_{1/3}Nb_{2/3})_{1-x}Ti_x]O_3$ single crystals studied by Brillouin light scattering, Phys. Rev. B **82**, 104110 (2010).

[9] R. E. Cohen, Theory of ferroelectrics: A vision for the next decade and beyond, J. Phys. Chem. Solids **61**, 139 (2000).

[10] B. Noheda, D. E. Cox, G. Shirane, J. Gao, and Z.-G. Ye, Phase diagram of the ferroelectric relaxor $(1-x)PbMg_{1/3}Nb_{2/3}O_{3-x}PbTiO_3$, Phys. Rev. B **66**, 054104 (2002).

[11] Y. Guo, H. Luo, K. Chen, H. Xu, X. Zhang, and Z. Yin, Effect of composition and poling field on the properties and ferroelectric phase-stability of $Pb(Mg_{1/3}Nb_{2/3})O_3$-$PbTiO_3$ crystals, J. Appl. Phys. **92**, 6134 (2002).

[12] Y. Guo, H. Luo, D. Ling, H. Xu, T. He, and Z. Yin, The phase transition sequence and the location of the morphotropic phase boundary region in $(1-x)[Pb(Mg_{1/3}Nb_{2/3})O_3]$-$xPbTiO_3$ single crystal, J. Phys.: Condens. Matter **15**, L77 (2003).

[13] J. H. Qiu, J. N. Ding, N. Y. Yuan, and X. Q. Wang, Phase diagram of $(1-x)PbMg_{1/3}Nb_{2/3}O_{3-x}PbTiO_3$ single crystals, J. Appl. Phys. **117**, 74101 (2015).

[14] M. A. Carpenter, J. F. J. Bryson, G. Catalan, S. J. Zhang, and N. J. Donnelly, Elastic and anelastic relaxations in the relaxor ferroelectric $Pb(Mg_{1/3}Nb_{2/3})O_3$: II. Strain-order parameter coupling and dynamic softening mechanisms, J. Phys.: Condens. Matter **24**, 45902 (2012).

[15] D. Fu, H. Taniguchi, M. Itoh, and S. Mori, $Pb(Mg_{1/3}Nb_{2/3})O_3$ (PMN) relaxor: Dipole glass or nano-domain ferroelectric? Adv. Ferroelectr. **3**, 8 (2012).

[16] F. Cordero, Elastic properties and enhanced piezoelectric response at morphotropic phase boundaries, Mater. (Basel) **8**, 8195 (2015).

[17] Y. Chen, K. H. Lam, D. Zhou, Q. Yue, Y. Yu, J. Wu, W. Qiu, L. Sun, C. Zhang, H. Luo, H. L. W. Chan, and J. Dai, High performance relaxor-based ferroelectric single crystals for ultrasonic transducer applications, Sensors (Basel) **14**, 13730 (2014).

[18] M. Ahart, A. Asthagiri, Z.-G. Ye, P. Dera, H. Mao, R. E. Cohen, and R. J. Hemley, Brillouin scattering and molecular dynamics study of the elastic properties of $Pb(Mg_{1/3}Nb_{2/3})O_3$, Phys. Rev. B **75**, 144410 (2007).

[19] M. Ghasemifard, S. M. Hosseini, and G. H. Khorrami, Synthesis and structure of PMN-PT ceramic nanopowder free from pyrochlore phase, Ceram. Int. **35**, 2899 (2009).

[20] W. D. Dong, P. Finkel, A. Amin, and C. S. Lynch, Giant electromechanical energy conversion in [011] cut ferroelectric single crystals, Appl. Phys. Lett. **100**, 042903 (2012).

[21] Y. Lu, D. Y. Jeong, Z. Y. Cheng, Q. M. Zhang, H. S. Luo, Z. W. Yin, and D. Viehland, Phase transitional behavior and piezoelectric properties of the orthorhombic phase of $Pb(Mg_{1/3}Nb_{2/3})O_3$-$PbTiO_3$ single crystals, Appl. Phys. Lett. **78**, 3109 (2001).

[22] A. K. Singh, D. Pandey, and O. Zaharko, Powder neutron diffraction study of phase transitions in and a phase diagram of $(1-x)[Pb(Mg_{1/3}Nb_{2/3})O_3]$-$xPbTiO_3$, Phys. Rev. B **74**, 024101 (2006).

[23] O. Noblanc, P. Gaucher, and G. Calvarin, Structural and dielectric studies of $Pb(Mg_{1/3}Nb_{2/3})O_3$-$PbTiO_3$ ferroelectric solid solutions around the morphotropic boundary, J. Appl. Phys. **79**, 4291 (1996).

[24] H. Fu and R. Cohen, Polarization rotation mechanism for ultrahigh electromechanical response in single-crystal piezoelectrics, Nature (London) **403**, 281 (2000).

[25] O. Svitelskiy, A. V. Suslov, J. B. Betts, A. Migliori, G. Yong, and L. A. Boatner, Resonant ultrasound spectroscopy of $KTa_{1-x}Nb_xO_3$ ferroelectric relaxor crystals, Phys. Rev. B **78**, 064113 (2008).

[26] G. Li and J. R. Gladden, High temperature resonant ultrasound spectroscopy: A review, Int. J. Spectrosc. **2010**, 206362 (2010).

[27] G. F. Nataf, Q. Li, Y. Liu, R. L. Withers, S. L. Driver, and M. A. Carpenter, Ferroelastic aspects of relaxor ferroelectric behaviour in $Pb(In_{1/2}Nb_{1/2})O_3$-$Pb(Mg_{1/3}Nb_{2/3})O_3$-$PbTiO_3$ perovskite, J. Appl. Phys. **113**, 124102 (2013).

[28] R. G. Leisure and F. A. Willis, Resonant ultrasound spectroscopy, J. Phys.: Condens. Matter **9**, 6001 (1997).

[29] A. Migliori and T. W. Darling, Resonant ultrasound spectroscopy for materials studies and non-destructive testing, Ultrasonics **34**, 473 (1996).

[30] X. Liu, S. Zhang, J. Luo, T. R. Shrout, and W. Cao, Complete set of material constants of $Pb(In_{1/2}Nb_{1/2})O_3$-$Pb(Mg_{1/3}Nb_{2/3})O_3$-$PbTiO_3$ single crystal with morphotropic phase boundary composition, J. Appl. Phys. **106**, 74112 (2009).

[31] H. Cao, V. H. Schmidt, R. Zhang, W. Cao, and H. Luo, Elastic, piezoelectric, and dielectric properties of $0.58Pb(Mg_{1/3}Nb_{2/3})O_3$-$0.42PbTiO_3$ single crystal, J. Appl. Phys. **96**, 549 (2004).

[32] R. Zhang, W. Jiang, B. Jiang, and W. Cao, Elastic, Dielectric and Piezoelectric Coefficients of Domain Engineered $0.70Pb(Mg_{1/3}Nb_{2/3})O_{3\text{-}0.30}PbTiO_3$ Single Crystal, in *Fundamental Physics of Ferroelectrics 2002*, AIP Conf. Proc. 626 (AIP, New York, 2002), pp. 188–197.

[33] J. Luo, W. Hackenberger, S. Zhang, and T. R. Shrout, Elastic, piezoelectric and dielectric properties of PIN-PMN-PT crystals grown by Bridgman method, in *Proceedings of IEEE Ultrasonics Symposium, IUS 2008* (IEEE, 2008).

[34] See Supplemental Material at http://link.aps.org/supplemental/10.1103/PhysRevB.96.134108 for powder x-ray diffraction data, high-temperature resonant ultrasound spectroscopy (RUS), pulse-echo experimental setup, and temperature dependence of sound wave velocities and Poisson's ratio.

[35] I. Ohno, Free vibration of a rectangular parallelepiped crystal and its application to determination of elastic constants of orthorhombic crystals, J. Phys. Earth **24**, 355 (1976).

[36] W. M. Visscher, A. Migliori, T. M. Bell, and R. A. Reinert, On the normal modes of free vibration of inhomogeneous and anisotropic elastic objects, J. Acoust. Soc. Am. **90**, 2154 (1991).

[37] O. O. L. Anderson, Rectangular parallelepiped resonance—A technique of resonance ultrasound and its applications to the determination of elasticity at high temperatures, J. Acoust. Soc. Am. **91**, 2245 (1992).

[38] A. Migliori and J. D. Maynard, Implementation of a modern resonant ultrasound spectroscopy system for the measurement of the elastic moduli of small solid specimens, Rev. Sci. Instrum. **76**, 121301 (2005).

[39] H. H. Demarest, Cube-resonance method to determine the

elastic constants of solids, J. Acoust. Soc. Am. **49**, 768 (1971).

[40] G. Li, *High Temperature Resonant Ultrasound Spectroscopy Studies of Thermoelectrics and Other Novel Materials* (University of Mississippi, University, MS, 2010).

[41] A. Lopez-Sanchez and L. W. Schmerr, *Characterization of an Ultrasonic Transducer in a Pulse-Echo Setup*, AIP Conf. Proc. No. 820 I (AIP, New York, 2006), p. 900.

[42] C. Pantea, D. G. Rickel, A. Migliori, R. G. Leisure, J. Zhang, Y. Zhao, S. El-Khatib, and B. Li, Digital ultrasonic pulse-echo overlap system and algorithm for unambiguous determination of pulse transit time, Rev. Sci. Instrum. **76**, 114902 (2005).

[43] H. W. King, S. H. Ferguson, D. F. Waechter, and S. E. Prasad, *An X-Ray Diffraction Study of PMNPT Ceramics near the Morphotropic Phase Boundary*, Proc. Int. Conf. Sonar-Sensors Syst., Kochi, India (Allied Publishers, New Delhi, 2002).

[44] J. Erhart and W. Cao, Effective material properties in twinned ferroelectric crystals, J. Appl. Phys. **86**, 1073 (1999).

[45] B. Noheda, Structure and high-piezoelectricity in lead oxide solid solutions, Curr. Opin. Solid State Mater. Sci. **6**, 27 (2002).

[46] M. Sepliarsky and R. E. Cohen, First-principles based atomistic modeling of phase stability in PMN-xPT, J. Phys.: Condens. Matter. **23**, 435902 (2011).

[47] A. Migliori and J. L. Sarrao, *Resonant Ultrasound Spectroscopy: Applications to Physics, Materials Measurements, and Nondestructive Evaluation* (Wiley-VCH, New York, 1997).

[48] D. H. Chung and W. R. Buessem, The Voigt-Reuss-Hill (VRH) approximation and the elastic moduli of polycrystalline ZnO, TiO_2 (rutile), and α-Al_2O_3, J. Appl. Phys. **39**, 2777 (1968).

[49] R. Hill, The elastic behaviour of a crystalline aggregate, Proc. Phys. Soc. Sect. A **65**, 349 (1952).

[50] J. W. Jaeken and S. Cottenier, Solving the Christoffel equation: Phase and group velocities, Comput. Phys. Commun. **207**, 445 (2016).

[51] F. I. Fedorov, *Theory of Elastic Waves in Crystals* (Springer, Boston, 1968).

[52] S. Zhang, F. Li, N. P. Sherlock, J. Luo, H. J. Lee, R. Xia, R. J. Meyer, W. Hackenberger, and T. R. Shrout, Recent developments on high Curie temperature PIN-PMN-PT ferroelectric crystals, J. Cryst. Growth **318**, 846 (2011).

[53] C. S. Pandey, J. Schreuer, M. Burianek, and M. Mühlberg, Anomalous elastic behavior of relaxor ferroelectric $Ca_{0.28}Ba_{0.72}Nb_2O_6$ single crystals, Phys. Rev. B **84**, 174102 (2011).

[54] C. S. Pandey, J. Schreuer, M. Burianek, and M. Mühlberg, Relaxor behavior of $Ca_xBa_{1-x}Nb_2O_6$ ($0.18 \leqslant x \leqslant 0.35$)) tuned by Ca/Ba ratio and investigated by resonant ultrasound spectroscopy, Phys. Rev. B **87**, 094101 (2013).

[55] M. A. Carpenter, A. Buckley, P. A. Taylor, and T. W. Darling, Elastic relaxations associated with the Pm3m-R3c transition in $LaAlO_3$: III. Superattenuation of acoustic resonances, J. Phys.: Condens. Matter. **22**, 35405 (2010).

[56] W. Ren, L. Han, R. Wicks, G. Yang, and B. K. Mukherjee, Electric-field-induced phase transitions of ⟨001⟩-oriented $Pb(Mg_{1/3}Nb_{2/3})O_3$-$PbTiO_3$ single crystals, in *Proc. SPIE 5761, Smart Structures and Materials 2005: Active Materials: Behavior and Mechanics* (SPIE, 2005).

[57] L. Bellaiche and D. Vanderbilt, Intrinsic Piezoelectric Response in Perovskite Alloys: PMN-PT Versus PZT, Phys. Rev. Lett. **83**, 1347 (1999).

[58] G. A. Smolenskii, N. K. Yushin, and S. I. Smirnov, Acoustic properties of the lead magnoniobate crystal as a ferroelectric with a smeared phase transition region, Fiz. Tverd. Tela **27**, 801 (1985).

[59] A. I. Fedoseev and S. G. Lushnikov, Elastic properties of cubic relaxor ferroelectrics, Bull. Russ. Acad. Sci. Phys. **72**, 1436 (2008).

[60] S. G. Lushnikov, A. I. Fedoseev, S. N. Gvasaliya, and S. Kojima, Anomalous dispersion of the elastic constants at the phase transformation of the $PbMg_{1/3}Nb_{2/3}O_3$ relaxor ferroelectric, Phys. Rev. B **77**, 104122 (2008).

[61] A. G. Kalinichev, J. D. Bass, B. N. Sun, and D. A. Payne, Elastic properties of tetragonal $PbTiO_3$ single crystals by Brillouin scattering, J. Mater. Res. **12**, 2623 (1997).

[62] M. K. Fig, MATLAB Software Calculates Resonant Frequencies and Mode Shapes for RUS, https://www.mathworks.com/matlabcentral/fileexchan (2008).

[63] S. W. Choi, R. T. R. Shrout, S. J. Jang, and A. S. Bhalla, Dielectric and pyroelectric properties in the $Pb(Mg_{1/3}Nb_{2/3})O_3$-$PbTiO_3$ system, Ferroelectrics **100**, 29 (1989).

[64] J. B. Li, G. Rao, G. Liu, J. Chen, L. Lu, X. Jing, S. Li, and J. Liang, Structural transition in unpoled (1-x)PMN-xPT ceramics near the morphotropic boundary, J. Alloys Compd. **425**, 373 (2006).